European Journal of Medicinal Chemistry 207 (2020) 112848

Contents lists available at ScienceDirect

European Journal of Medicinal Chemistry

journal homepage: http://www.elsevier.com/locate/ejmech

Research paper

Structure-guided optimization and mechanistic study of a class of quinazolinone-threonine hybrids as antibacterial ThrRS inhibitors

Junsong Guo, Bingyi Chen, Ying Yu, Bao Cheng, Yingchen Ju, Jieyu Tang, Zhengjun Cai, Qiong Gu, Jun Xu, Huihao Zhou*

Research Center for Drug Discovery and Guangdong Provincial Key Laboratory of Chiral Molecule and Drug Discovery, School of Pharmaceutical Sciences, Sun Yat-sen University, Guangzhou, 510006, China

ARTICLE INFO

Article history:
Received 24 June 2020
Received in revised form
12 August 2020
Accepted 12 September 2020
Available online 19 September 2020

Keywords:
Structure-based drug design
Aminoacyl-tRNA synthetase
Molecular mechanism
Antimicrobial

ABSTRACT

Aminoacyl-tRNA synthetases (aaRSs) are an attractive class of antibacterial drug targets due to their essential roles in protein translation. While most traditional aaRS inhibitors target the binding pockets of substrate amino acids and/or ATP, we recently developed a class of novel tRNA-amino acid dual-site inhibitors including inhibitor **3** ((2*S*,3*R*)-2-amino-*N*-((*E*)-4-(6,7-dichloro-4-oxoquinazolin-3(4*H*)-yl)but-2-en-1-yl)-3-hydroxybutanamide) against threonyl-tRNA synthetase (ThrRS). Here, the binding modes and structure-activity relationships (SARs) of these inhibitors were analyzed by the crystal structures of *Salmonella enterica* ThrRS (*Se*ThrRS) in complex with three of them. Based on the cocrystal structures, twelve quinazolinone-threonine hybrids were designed and synthesized, and their affinities, enzymatic inhibitory activities, and cellular potencies were evaluated. The best derivative **8g** achieved a K_d value of 0.40 μM, an IC_{50} value of 0.50 μM against *Se*ThrRS and MIC values of 16–32 μg/mL against the tested bacterial strains. The cocrystal structure of the *Se*ThrRS-**8g** complex revealed that **8g** induced a bended conformation for Met332 by forming hydrophobic interactions, which better mimicked the binding of $tRNA^{Thr}$ to ThrRS. Moreover, the inhibitory potency of **8g** was less impaired than a reported ATP competitive inhibitor at high concentrations of ATP, supporting our hypothesis that tRNA site inhibitors are likely superior to ATP site inhibitors *in vivo*, where ATP typically reaches millimolar concentrations.

1. Introduction

Ribosomes use aminoacyl-tRNAs as substrates to decode mRNAs and synthesize peptides during protein translation [1,2], and the ligation of amino acids to their cognate tRNAs is catalyzed by a group of ancient enzymes named aminoacyl-tRNA synthetases (aaRSs) [2,3]. Due to the essentiality of protein translation in various life processes, inhibition of aaRSs results in the death of pathogenic bacteria [4–8]. Moreover, the structures and mechanisms of aaRSs have been deeply studied in recent decades, providing great opportunities for the development of clinically useful aaRS inhibitors to fight microbial infections (Fig. 1) [7,9–22].

Threonyl-tRNA synthetase (ThrRS) is an aaRS family member that links L-threonine (L-Thr) to $tRNA^{Thr}$ [23]. It catalyzes a two-step reaction to synthesize threonyl-$tRNA^{Thr}$: 1) L-Thr is activated by ATP to form a threonyl-AMP intermediate; and 2) the threonyl moiety of the intermediate is transferred to nucleotide A76 of the 3' CCA-end of $tRNA^{Thr}$ [21,24]. Most reported inhibitors of ThrRS and other aaRS members competitively disturb the formation of the first step aminoacyl-AMP intermediates by occupying the binding pockets of the amino acid and/or ATP substrates, such as the non-hydrolyzable analogs of the aminoacyl-AMP intermediates (Fig. 1, **VII** and **VIII**) [21,22,25]. Despite promising affinities and activities at the target level, these nonhydrolyzable analog inhibitors usually lack sufficient activity against bacterial cells; thus, they have rarely entered into clinical trials [26–28]. There are at least two possible reasons to explain why these traditional aaRS inhibitors are not potent at the cellular level [29,30]. First, the low membrane permeability of these inhibitors prevents them from being efficiently transported across cell membranes to give a cellular response. Second, the ATP concentration increases by 2–3 orders of magnitude in bacterial cells (1–10 mM) compared to *in vitro* enzymatic assays (typically 1–10 μM), making the ATP substrate compete strongly with these inhibitors *in vivo* [31].

While the concentration of each tRNA is significantly lower than

* Corresponding author.
E-mail address: zhuihao@mail.sysu.edu.cn (H. Zhou).

https://doi.org/10.1016/j.ejmech.2020.112848
0223-5234/

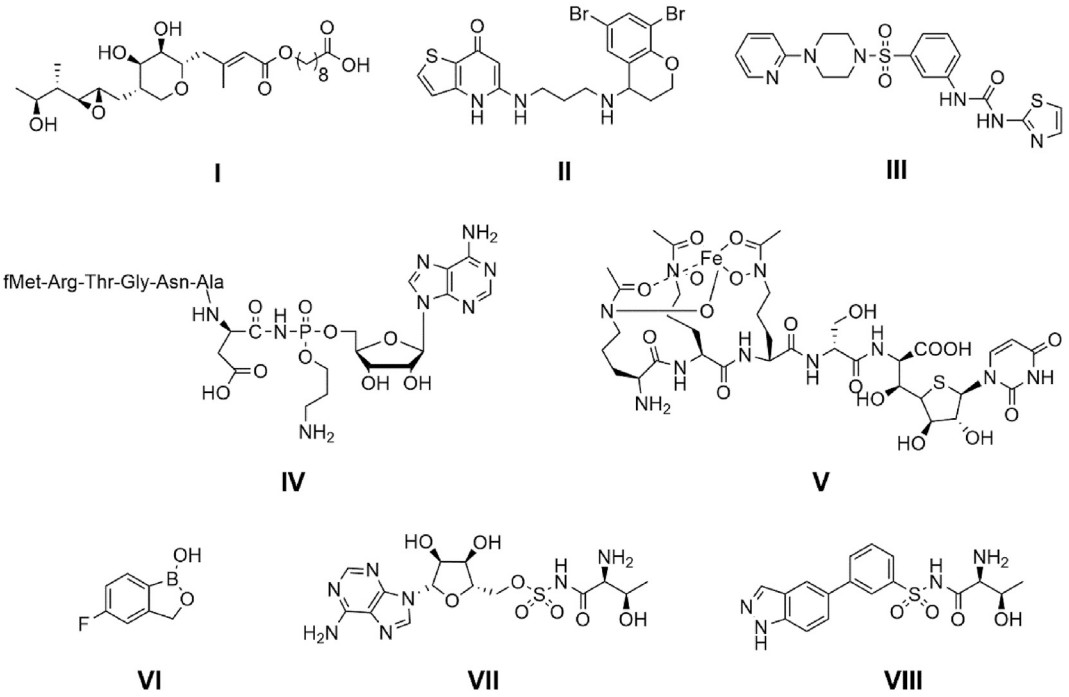

Fig. 1. Representative inhibitors of aaRS: Mupirocin (**I**), REP3123 (**II**), GAX (**III**), Microcin C (**IV**), Albomycin (**V**), AN2690 (**VI**), Thr-AMS (**VII**), and **11d** (**VIII**).

that of ATP in bacterial cells, inhibitors targeting the binding pocket of substrate tRNA are likely easier to inhibit the aminoacylation activities of aaRSs compared to traditional ATP-competitive inhibitors. In addition, targeting the binding pocket of $tRNA^{Thr}$ could open up a new mechanism and reveal a new skeleton for ThrRS inhibitors to overcome potential drug resistance. Recently, we developed a series of tRNA-amino acid dual-site ThrRS inhibitors based on a fragment-based target hopping approach to simultaneously target the binding pockets of $tRNA^{Thr}$ and L-Thr of ThrRS, which is a novel mechanism compared to all other reported ThrRS inhibitors [32]. Considering the plasticity of the active site of bacterial ThrRS, developing effective ThrRS tRNA site inhibitors requires further tuning of the interactions between the inhibitors and the conserved residues around the active site.

Here, the crystal structures of *Salmonella enterica* ThrRS (*Se*ThrRS) in complex with inhibitors **1**, **2** and **3** were analyzed, and the interactions between the inhibitors and *Se*ThrRS were thoroughly analyzed. Then, a new set of quinazolinone-threonine hybrids was designed and synthesized, and their biochemical properties, enzymatic inhibitory activities, binding modes, and cellular potencies were studied.

2. Results

2.1. Crystal structures of the SeThrRS-inhibitor complexes and SAR analysis

We previously reported that tRNA-amino acid dual-site *Se*ThrRS inhibitors featured a halogenated quinazolinone ring linked by a hydrophobic chain to the L-Thr moiety (Fig. 2) [32]. We were interested in the detailed binding mechanisms and the structure-activity relationships (SARs) of these inhibitors, which would give essential insights into improving inhibitory potency. *Se*ThrRS was separately crystallized with inhibitors **1**, **2** and **3**, and X-ray crystallography provided unambiguous electron density maps for these inhibitors in the *Se*ThrRS active site.

In the crystal structure of *Se*ThrRS with inhibitor **1** (Fig. 3A), the halogenated quinazolinone moiety occupied a similar site as A76 of $tRNA^{Thr}$. The planar halogenated quinazolinone moiety was inserted into the $tRNA^{Thr}$ binding pocket of *Se*ThrRS mainly through π-π stacking interactions with Tyr313 and cation-π interactions with Arg363. In addition, several other residues within the $tRNA^{Thr}$ binding pocket, including Ala316, Met317 and Pro331, contributed important hydrophobic interactions to stabilize inhibitor **1**. Within the L-Thr binding pocket, Zn^{2+} coordinated by Cys334, His385 and His511 formed two important coordination bonds with the α-NH_2 and β-OH of inhibitor **1**. Moreover, structural water-mediated hydrogen bonding interactions between inhibitor **1** and residues Gln381 and Asp383 were observed.

By replacing the five-carbon alkyl linker of inhibitor **1** with (*E*)-but-2-ene, inhibitor **2** showed a 19-fold improvement in inhibitory potency (Fig. 2). The largest difference between the binding modes of inhibitors **1** and **2** was that the conformation of the quinazolinone moiety of inhibitor **2** flipped over 90° with respect to inhibitor **1** (Fig. 3B and C). Thus, the quinazolinone moiety of inhibitor **2** formed more favorable interactions with the positively charged Arg363, and the suitable length of the four-carbon linker of inhibitor **2** played an important role in optimally orienting the quinazolinone moiety. In addition, the linker of inhibitor **2** with the conjugated system was less rotatable than the linker of inhibitor **1**, suggesting that inhibitor **2** is endowed with a lower conformational entropy. Therefore, the loss of entropy of inhibitor **2** was likely lower than that of inhibitor **1** after binding to *Se*ThrRS, contributing to an overall more favorable binding energy. Indeed, inhibitor **2** showed more stable binding poses (especially the linker region) and better energy scores compared to inhibitor **1** in the flexible molecular docking experiments (Fig. S1). Inhibitor **3** was also crystallized with *Se*ThrRS (Fig. 3D) [32]. Inhibitor **3** bound in a very similar binding mode compared to inhibitor **2** but the inhibitory activity of **3** was approximately 7-fold better than that of **2**, which might be because the quinazolinone moiety of inhibitor **3** formed more hydrophobic contacts with conserved residues Ala316 and Met317 at the distal side of the $tRNA^{Thr}$ binding pocket.

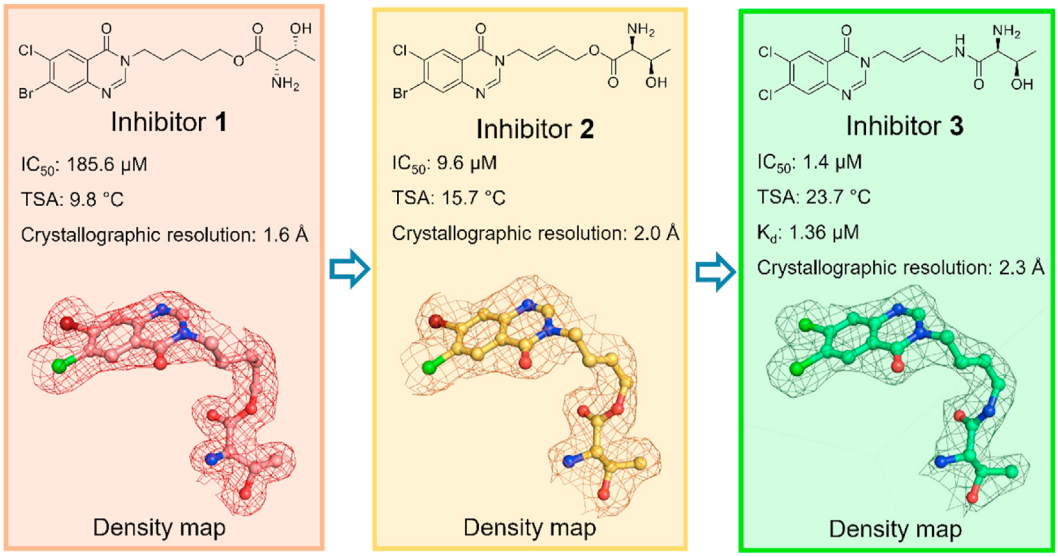

Fig. 2. The evolution of inhibitor **3** from inhibitor **1**. The chemical structures, enzymatic inhibitory activities, affinities and X-ray crystallographic structures of inhibitors **1**, **2** and **3**.

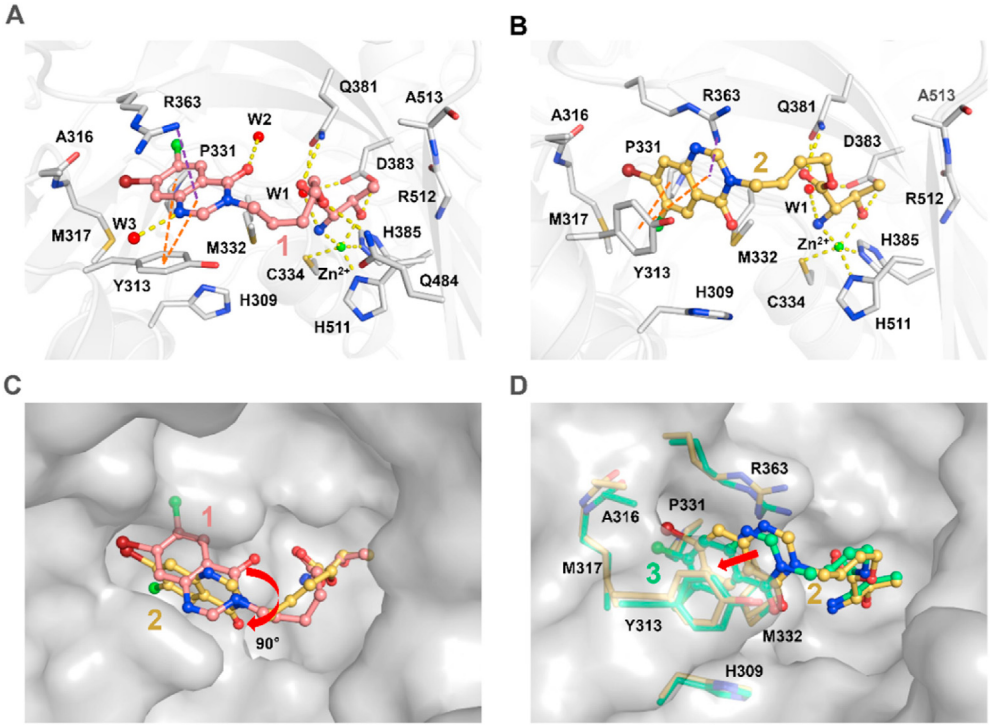

Fig. 3. Crystal structures of *Se*ThrRS in complex with inhibitors. (A) The binding mode of inhibitor **1** (pink, PDB code: 7CBI). (B) The binding mode of inhibitor **2** (light yellow, PDB code: 7CBH). (C) Conformational comparison between inhibitors **1** and **2** in the active site of *Se*ThrRS. (D) Conformational comparison between inhibitors **2** and **3** (green, PDB code: 6L2P) in the active site of *Se*ThrRS. Water molecules are shown as red spheres; zinc ions are shown as light green spheres; hydrogen bonds are shown as yellow dashed lines; cation-π interactions are shown as purple dashed lines; and π - π stacking interactions are shown as orange dashed lines. (For interpretation of the references to colour in this figure legend, the reader is referred to the Web version of this article.)

2.2. Structure-guided optimization of inhibitors

Previous studies showed that the L-Thr binding pocket of ThrRS is highly specific for the substrate L-Thr, and all modifications to the L-Thr moiety did not improve the affinities of the inhibitors [22]. However, the *Se*ThrRS-inhibitor **3** crystal structure suggested that the L-Thr moiety could still undergo reasonable modifications to better fit in the binding pocket. Therefore, larger cyclic fragments with similar spatial conformations to the L-Thr moiety (compounds **8a-b**), a different chirality of threonine moiety (compound **8c**) and some slight modifications to the L-Thr moiety (compounds **8d-f**) were investigated to find a new direction for improving the potency of inhibitor **3**.

Moreover, Met332, a residue located at the boundary between the binding pockets of $tRNA^{Thr}$ and L-Thr, adopted a bent conformation to enlarge the pocket for accommodating A76 of $tRNA^{Thr}$ in

the ThrRS-tRNA^{Thr} complex, but Met332 remained in an extended conformation after binding inhibitor **3** (Fig. 4A and B) [32–34]. After A76 of tRNA^{Thr} entered the pocket, the hydrophobic side chain of Met332 was pushed away, possibly by the ribose moiety of A76 of tRNA^{Thr} (Fig. 5A). The chemically modifiable α-NH_2 of the inhibitors faced Met332, which provided an opportunity for designing structural analogs that could form additional protein contacts and induce a bended conformation of Met332 to better mimic the binding of the substrate tRNA^{Thr} (Fig. 5B). Thus, while keeping the coordination bonds with Zn^{2+}, a methyl group was placed on the α-NH_2 of the L-Thr moiety (compound **8g**). After testing the activities of compounds **8a-g**, the inhibitory potency of compound **8g** was improved against *Se*ThrRS compared to parent inhibitor **3**. Therefore, we introduced different single alkyl substitutions onto the α-NH_2 of the L-Thr moiety (compounds **9a-e**) to further explore modifications to inhibitor **3**.

Flexible molecular docking calculations of all the designed compounds were performed, and their best binding poses and energetic scores are provided in the Supplementary Information (Supplementary Figs. S2 and S3).

2.3. Chemistry

The synthesis of quinazolinone-threonine hybrids is outlined in Scheme 1. The chlorinated quinazolinone ring (**5**) was constructed from compound **4** in the presence of formamide followed by alkylation with (*E*)-1,4-dibromobut-2-ene to produce compound **6** [35,36]. Subsequently, compound **6** was converted to the corresponding azide intermediate, which was then reduced in the presence of triphenylphosphine to give compound **7** [37,38]. After a coupling reaction with 5-oxopyrrolidine-2-carboxylic acid, Boc-L-Thr or Boc-protected threonine analogs followed by deprotection of the Boc group, compound **7** was converted to inhibitor **3** and compounds **8a-g** [22,39]. Inhibitor **3** was introduced a variety of alkyl chains onto the α-NH_2 of the L-Thr moiety under basic conditions to yield compounds **9a-e**. Details of the synthesis of the compounds are given in experimental section 4.2.

2.4. Biological evaluation of the designed compounds at the enzymatic level

Heating a protein will cause thermal denaturation at a certain temperature (T_m), and compound binding could stabilize the protein and increase its melting temperature ($\Delta T_m = T_{m\_compound\ binding} - T_{m\_apo}$) [40,41]. The ΔT_m caused by a compound is positively correlated to its affinity [42]. The T_m values of *Se*ThrRS were measured with or without 0.5 mM each compound by employing fluorescence-based thermal shift assays (TSAs) (Table 1). Conversion of the L-Thr skeleton to the corresponding lactams (compounds **8a** and **8b**) was not tolerated against *Se*ThrRS. Exchanging the L-configuration for the D-configuration (compound **8c**) resulted in negligible affinity. The effect of the addition or removal of the terminal methyl group (compounds **8d** and **8e**, respectively) resulted in a sharp drop in affinity. Modifying the β-OH of inhibitor **3** to a β-methoxyl group (compound **8f**) led to a complete loss of affinity. These modifications to the L-Thr moiety might interfere with the compounds reaching the L-Thr binding pocket of *Se*ThrRS and were sensitized to the enzyme affinities.

The data revealed that the binding affinity of compound **8g** ($\Delta T_m = 28.4\ ^\circ C$) was improved against *Se*ThrRS compared to parent inhibitor **3** ($\Delta T_m = 23.7\ ^\circ C$). The possible reason for the stronger binding of compound **8g** was that the nitrogen atom of α-methylamine group carried more electrons donated by the methyl group and could form a stronger coordination bond with Zn^{2+} than inhibitor **3**. Moreover, the increased affinity of compound **8g** might also be caused by **8g** forming additional interactions near the tRNA^{Thr} binding pocket of *Se*ThrRS.

The inhibitory activities of these compounds against *Se*ThrRS were determined by using the luciferase ATP consumption assay, and the results are summarized in Table 1. The inhibition rates of the compounds were evaluated at a concentration of 100 μM, and the IC_{50} values were further measured for the compounds with inhibition rates greater than 50% at 100 μM (Fig. S4). Consistent with the TSA results, the inhibitory activities of these compounds against *Se*ThrRS were sensitive to minor modifications of the L-Thr moiety. When the L-Thr moiety was converted to a lactam or D-threonine (compounds **8a**, **8b** and **8c**), these compounds exhibited negligible enzymatic inhibitory activity. Compound **8f** with, the β-OH decorated with a methyl group, was not tolerated, while the L-Thr moiety added or removed a terminal methyl group (compounds **8d** and **8e**, respectively) resulted in poor inhibition against *Se*ThrRS. Compound **8g** ($IC_{50} = 0.50$ μM) was approximately 3-fold more potent than parent inhibitor **3**. Importantly, successful modification of the α-NH_2 of the L-Thr moiety identified a new direction for subsequent compound structure modification.

As indicated in Table 2 and Fig. S4, we synthesized a series of compound **8g** analogs in which the α-NH_2 was alkylated with a variety of bulkier substituents in order to form optimal contacts with the residues near the tRNA^{Thr} binding pocket of *Se*ThrRS. Most analogs showed similar or increased affinities and inhibitory activities against *Se*ThrRS compared to parent inhibitor **3**, but their IC_{50} values were slightly weaker than compound **8g**. These data indicated that larger hydrophobic substituents on the α-NH_2 were not well tolerated, possibly due to potential steric clashes with the active site residues.

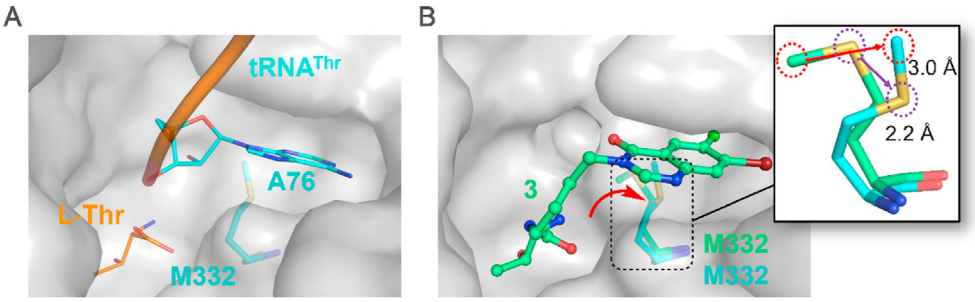

Fig. 4. Shape of the active site of *Se*ThrRS bound with different ligands. (A) tRNA^{Thr} (cyan) and L-Thr (orange) bound to the active site of ThrRS. (B) Inhibitor **3** (green) bound to the active site of ThrRS. Close-up view of Met332 in the tRNA^{Thr}-bound state (cyan) and the **3**-bound state (green). For Met332 in two states, a distance of 3 Å was calculated for the positions of its terminal methyl group and a distance of 2.2 Å was calculated for the positions of its sulfur atom. (For interpretation of the references to colour in this figure legend, the reader is referred to the Web version of this article.)

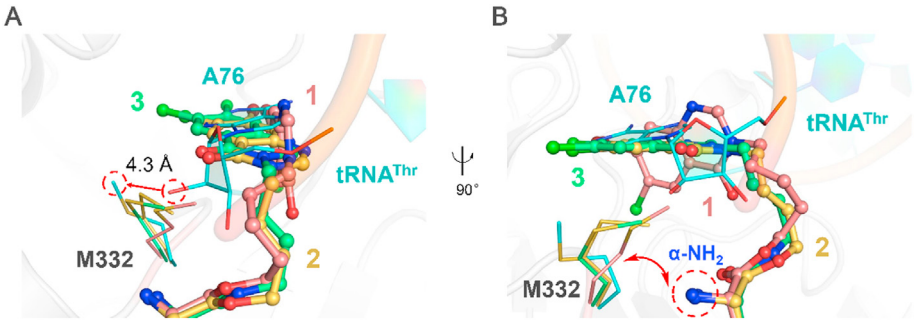

Fig. 5. Conformational comparison of the side chain of Met332 induced by inhibitors **1** (pink), **2** (light yellow), **3** (green) and A76 of $tRNA^{Thr}$ (cyan). (A) A distance of 4.3 Å was calculated between the terminal methyl group of Met332 and the hydroxyl group of A76 in the $tRNA^{Thr}$-bound state. (B) The chemically modifiable α-NH_2 of the inhibitors faced Met332. Introducing substituents onto the α-NH_2 of inhibitor **3** to induce the preferred conformation of Met332 found in the $tRNA^{Thr}$-bound state. (For interpretation of the references to colour in this figure legend, the reader is referred to the Web version of this article.)

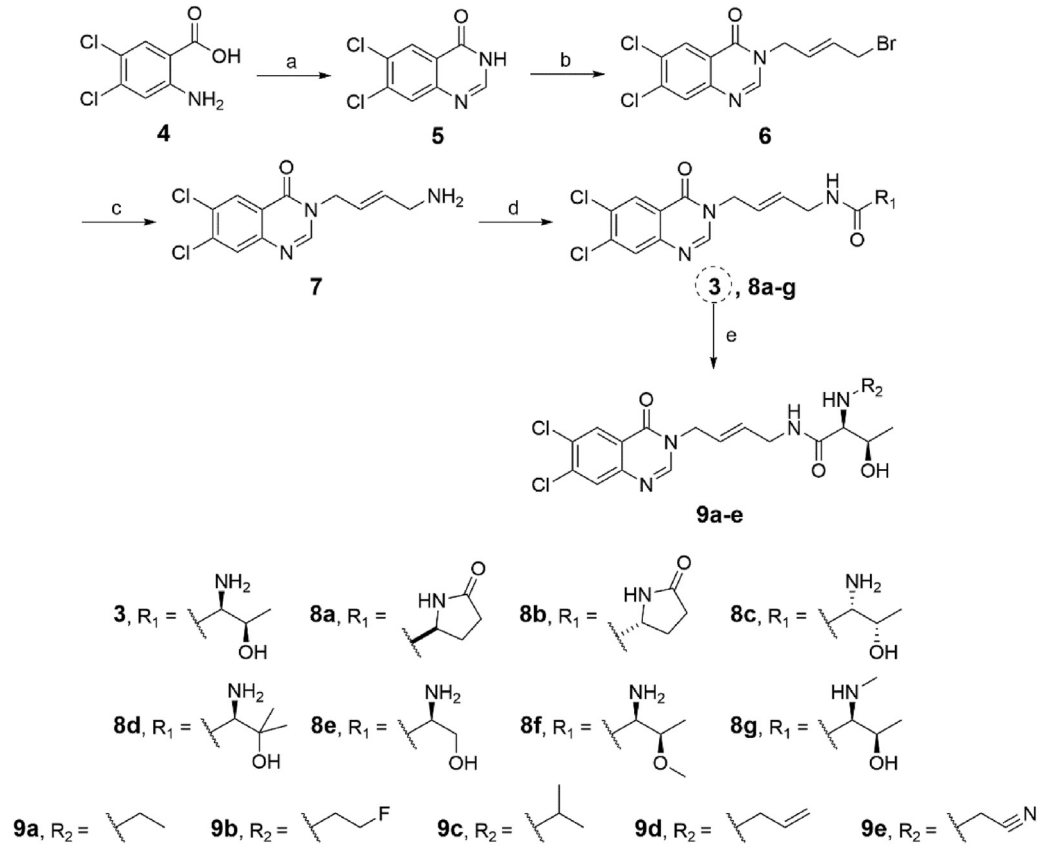

Scheme 1. Reagents and conditions: (a) formamide, 130 °C, overnight, 62%. (b) (*E*)-1,4-dibromobut-2-ene, K_2CO_3, DMF, rt, 2 h, 62%. (c) (i) CuI, sodium azide, DMSO, rt, 0.5 h, 93% (crude); (ii) triphenylphosphine, THF/H_2O = 5:1, rt, overnight, 85%. (d) (i) Boc-L-Thr, 5-oxopyrrolidine-2-carboxylic acid or Boc-protected threonine analogs, HATU, DIPEA, DMF, rt, 2 h, 84%–92%; (ii) 4 M HCl in dioxane, rt, 2 h, 85%–88%. (e) R_2I, NaH, DMF, rt, 6 h, 25%–78%.

To further assess affinity, we measured the disassociation constant (K_d) of compound **8g** against *Se*ThrRS using isothermal titration calorimetry (ITC, Fig. 6). Compound **8g** (200 μM) was titrated into 20 μM *Se*ThrRS, and the titration isotherm of compound **8g** in buffer was used as the baseline. By using the one-site equilibrium binding model, the K_d of compound **8g** to *Se*ThrRS was determined to be 0.40 μM. Thus, introducing the methyl group on the α-NH_2 afforded an approximately 3-fold increase in affinity compared to parent inhibitor **3** (K_d = 1.36 μM) [32].

2.5. Determination of the inhibitory mechanism of compound **8g**

The inhibition rate of compound **8g** against *Se*ThrRS was tested in the presence of various concentrations of substrates. The enzymatic activity of *Se*ThrRS inhibited by compound **8g** (10 μM) gradually recovered when the concentration of L-Thr progressively increased (Fig. 7A). Similarly, $tRNA^{Thr}$ and ATP also showed concentration-dependent recoveries of the enzymatic activity of *Se*ThrRS (Fig. 7B and C). These results revealed that compound **8g**

Table 1
The thermostabilization capability and inhibitory activity of compounds 8a-g against SeThrRS.

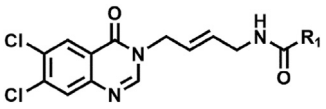

Compound	R_1 replacement	ΔT_m (°C)[a]	Inhibition rate (%)[b]	IC_{50} (μM)[c]
8a	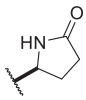	−0.4	5	NT[d]
8b		−0.2	0	NT
8c		0.6	6	NT
8d		0.9	0	NT
8e		0.6	2	NT
8f		0.2	4	NT
8g	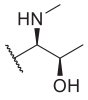	28.4	100	0.50
VIII[e]		29.7	100	0.14
HF[f]		−1.5	4	NT

[a] ΔT_m is the difference between the T_m values of *Se*ThrRS with and without 0.5 mM compound. The data are the average of three independent experiments.
[b] Inhibition rate represents the ratio of the loss in enzymatic activity after treatment with 100 μM compound. The data are the average of three independent experiments.
[c] IC_{50} values represent the half maximal (50%) inhibitory concentration. The data are the average of three independent experiments.
[d] NT, not tested.
[e] **VIII**: The reported inhibitor **11d** (Fig. 1) was used as a positive control [22].
[f] HF: ProRS inhibitor halofuginone (HF) was used as a negative control [43].

Table 2
The thermostabilization capability and inhibitory activity of compounds 9a-e against SeThrRS.

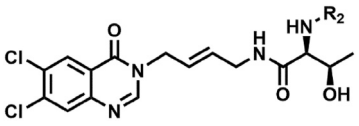

Compound	R_2 replacement	ΔT_m (°C)[a]	Inhibition rate (%)[b]	IC_{50} (μM)[c]
9a		22.5	100	0.96
9b		19.1	99	2.5
9c		14.1	63	49.3
9d		22.1	100	1.2
9e		18.8	93	9.6
VIII[d]		29.7	100	0.14
HF[e]		−1.5	4	NT[f]

[a] ΔT_m is the difference between the T_m values of *Se*ThrRS with and without 0.5 mM compound. The data are the average of three independent experiments.
[b] Inhibition rate represents the ratio of the loss in enzymatic activity after treatment with 100 μM compound. The data are the average of three independent experiments.
[c] IC_{50} values represent the half maximal (50%) inhibitory concentration. The data are the average of three independent experiments.
[d] **VIII**: The reported inhibitor **11d** (Fig. 1) was used as a positive control [22].
[e] HF: ProRS inhibitor HF was used as a negative control [43].
[f] NT, not tested.

competed with all three substrates simultaneously. However, interestingly, the inhibitory activity of compound **8g** against *Se*ThrRS was less impaired by high concentrations of ATP compared to the traditional ATP-amino acid dual-site inhibitor **VIII** (Figs. 1 and 7C), suggesting that compound **8g** and its analogs are potentially superior to traditional ThrRS inhibitors in bacterial cells where the ATP concentration usually reaches the millimolar range.

The crystal structure of *Se*ThrRS in complex with compound **8g** was then solved, and the electron density for compound **8g** was clear (Fig. 8A). We then compared the structure of the *Se*ThrRS-**8g** complex with the structures of ThrRS bound with the substrates. The halogenated quinazolinone moiety of compound **8g** sat in the $tRNA^{Thr}$ binding pocket formed by His309, Tyr313, Ala316, Met317, Pro331, Met332 and Arg363, but it penetrated deeper into the pocket than A76 to form more interactions with residues His309, Ala316 and Met317 (Fig. 8B) [33]. The methyl-substituted L-Thr moiety was anchored into the L-Thr binding pocket by forming coordination bonds with Zn^{2+} (Fig. 8C) [34]. In addition, residues Gln381 and Asp383 formed direct or indirect hydrogen bonding interactions with compound **8g** mediated by structural water. Compound **8g** did not overlap with the substrate ATP (Fig. 8D); however, the linker of compound **8g** was close to the α-phosphate group of ATP, indicating potential steric clashes between compound **8g** and ATP [23]. Consistently, although AMPPNP, a non-hydrolyzable analog of ATP, was also supplemented in the crystallization process of the *Se*ThrRS-**8g** complex, no electron density for AMPPNP could be observed, supporting that ATP and compound **8g** cannot bind to ThrRS simultaneously. Moreover, Met332 underwent a conformational change similar to that was observed in the ThrRS-$tRNA^{Thr}$ structure, and the methyl group on the α-NH_2 of compound **8g** occupied an induced hydrophobic subpocket generated by the rotation of Met332 (Fig. 9). The methyl group on the α-NH_2 of compound **8g** formed additional hydrophobic interactions with Met332 which were not observed in the structure of the *Se*ThrRS-inhibitor **3** complex, providing one of the possible reasons why introduction of the methyl group improved inhibitory potency against *Se*ThrRS.

This structural information highlighted several hot spots that could be explored to improve potency for tRNA-amino acid dual-site inhibitors; for example, hydrophobic interactions with the Met332 pocket at the bottom of the $tRNA^{Thr}$ binding pocket, electronic stacking interactions with Tyr313 and Arg363, hydrophobic packing interactions with residues distal to the $tRNA^{Thr}$ binding pocket, and coordination bonds with conserved Zn^{2+} in the L-Thr binding pocket.

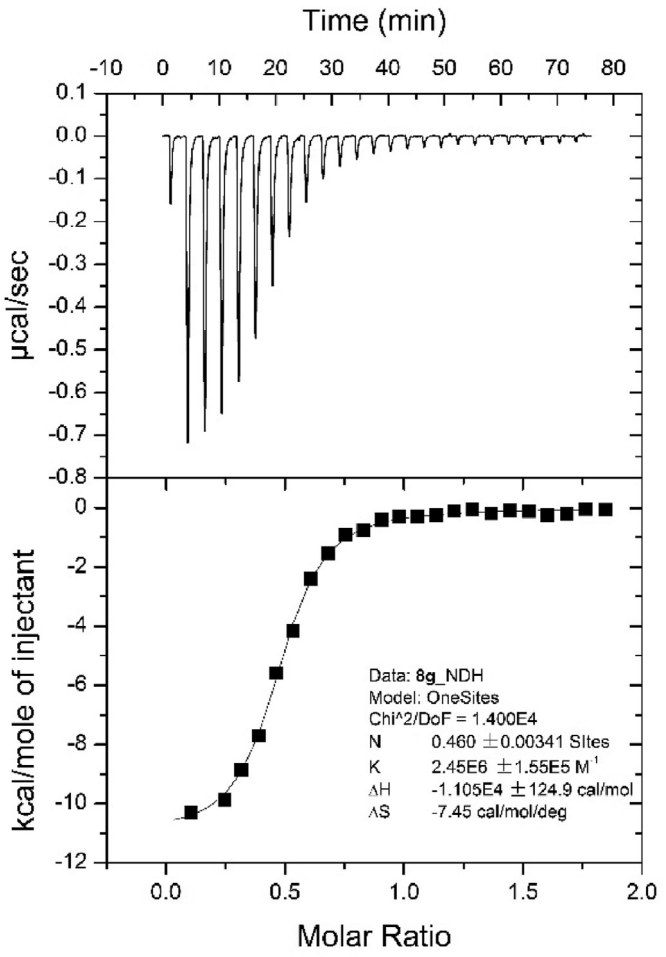

Fig. 6. ITC binding isotherms and integrated enthalpy plots for compound **8g** binding to *Se*ThrRS.

2.6. Antibacterial activity evaluation of the designed compounds at the cellular level

The minimum inhibitory concentration (MIC) was determined under Clinical and Laboratory Standards Institute (CLSI) conditions, with ampicillin and vancomycin as reference drugs (Table 3). Antibacterial testing against *Escherichia coli* ATCC25922 *in vitro* was performed for all the synthesized compounds, and compounds **8g**, **9a** and **9b** displayed detectable activity. Then, a wider panel of clinical pathogenic bacteria, including gram-positive bacterial strains (*Staphylococcus aure*us ATCC29213, methicillin-resistant *S. aureus* R3708 and *Enterococcus faecalis* ATCC29212) and gram-negative bacterial strains (*Salmonella enterica* 87 and *Pseudomonas aeruginosa* ATCC27853), was tested. The results showed that, in general, compounds **8g**, **9a** and **9b** had better inhibitory effects against gram-negative bacterial strains. The antibacterial potency decreases of these halogenated quinazolinone-threonine hybrids from enzyme to cells were much smaller than the traditional inhibitor **VIII**.

3. Conclusion

The crystal structures revealed the binding mode details of the tRNA-amino acid dual-site inhibitors **1**, **2** and **3** in the active site of *Se*ThrRS that can account for their inhibitory effects on this enzyme. This structural information guided the design of a set of new quinazolinone-threonine hybrids on the basis of inhibitor **3**. We found that adding a methyl or ethyl group on the α-NH_2 of the L-Thr moiety (compounds **8g** and **9a**) could improve the inhibitory activity. The following mechanistic studies revealed that the addition of the methyl group in compound **8g** induced the rotation of residue Met332 in the active site to better mimic the binding of the $tRNA^{Thr}$ substrate with ThrRS. These studies provide a basis for the further development of tRNA-amino acid dual-site aaRS inhibitors to treat infectious disease.

4. Experimental section

4.1. General chemistry

Chemicals were purchased from commercial sources and were used without further purification unless otherwise noted. Solvents were distilled prior to use. ^{1}H and ^{13}C NMR spectra were recorded on a Bruker 400 or Bruker 500 spectrometer using tetramethylsilane (TMS) as internal standard. The NMR data are displayed as follows: chemical shifts (δ) are recorded as ppm, coupling constants (J) in hertz (Hz), integration as the number of protons, and multiplicity as s (singlet), d (doublet), t (triplet), q (quartet), quintet, sextet, or m (multiplet). High-resolution mass spectra were recorded on a Shimadzu LCMS-IT-TOF mass spectrometer. Other mass spectra were recorded on a Shimadzu LCMS-2010A instrument with an ESI source. Flash column chromatography was performed using silica gel (200−300 mesh) purchased from Qingdao Haiyang Chemical Inc. All reaction progresses were monitored by thin layer chromatography (TLC) on GF254 precoated silica gel plates (Qingdao Haiyang Chemical Inc.), and the spots were detected under UV light (254 nm).

4.2. Synthetic procedures

4.2.1. Synthetic procedure for the preparation of intermediate *6*

To a stirred solution of **4** (2.00 g, 9.75 mmol) in formamide (30.0 mL) was heated to 130 °C overnight. The resulting mixture was quenched with water and precipitated crystals. The crude product was washed with brine (3 × 15.0 mL) and filtered to give intermediate **5**. A mixture of K_2CO_3 (1.67 g, 12.1 mmol) and **5** (1.30 g, 6.07 mmol) in anhydrous DMF (40.0 mL) was stirred at room temperature for 30 min. This white suspension was added (*E*)-1,4-dibromobut-2-ene (2.59 g, 12.1 mmol), and the resulting reaction mixture was stirred at room temperature for 2 h. The resulting mixture was quenched with water, and the aqueous solution was extracted with EtOAc (3 × 30.0 mL). The combined organic layers were washed with brine (3 × 30.0 mL), dried with anhydrous Na_2SO_4, filtered, and concentrated under vacuum to give the crude product. The crude product was purified by flash silica gel column chromatography (hexane/CH_2Cl_2 = 1/2) to afford **6** (1.30 g, 62%) as white crystals.

4.2.1.1. 6,7-dichloroquinazolin-4(3H)-one (**5**). Light brown crystals, 62%. ^{1}H NMR (400 MHz, DMSO) δ 12.75 (s, 1H), 9.10 (s, 1H), 8.33 (s, 1H), 7.72 (s, 1H). ESI-MS: m/z 215.0 $[M+H]^+$.

*4.2.1.2. (E)-3-(4-bromobut-2-en-*1-yl*)-6,7-dichloroquinazolin-4(3H)-one* (**6**). White crystals, 62%. ^{1}H NMR (400 MHz, $CDCl_3$) δ 8.37 (s, 1H), 8.00 (s, 1H), 7.84 (s, 1H), 5.98−5.91 (m, 2H), 4.63 (d, J = 5.3 Hz, 2H), 3.93 (d, J = 6.4 Hz, 2H). ESI-MS: m/z 346.9 $[M+H]^+$.

4.2.2. Synthetic procedure for the preparation of intermediate *7*

Compound **6** (1.30 g, 3.76 mmol), CuI (71.4 mg, 0.376 mmol) and sodium azide (293 mg, 4.51 mmol) were dissolved in DMSO (12.0 mL) and stirred at room temperature for 0.5 h. The resulting mixture was quenched with water, and the aqueous solution was

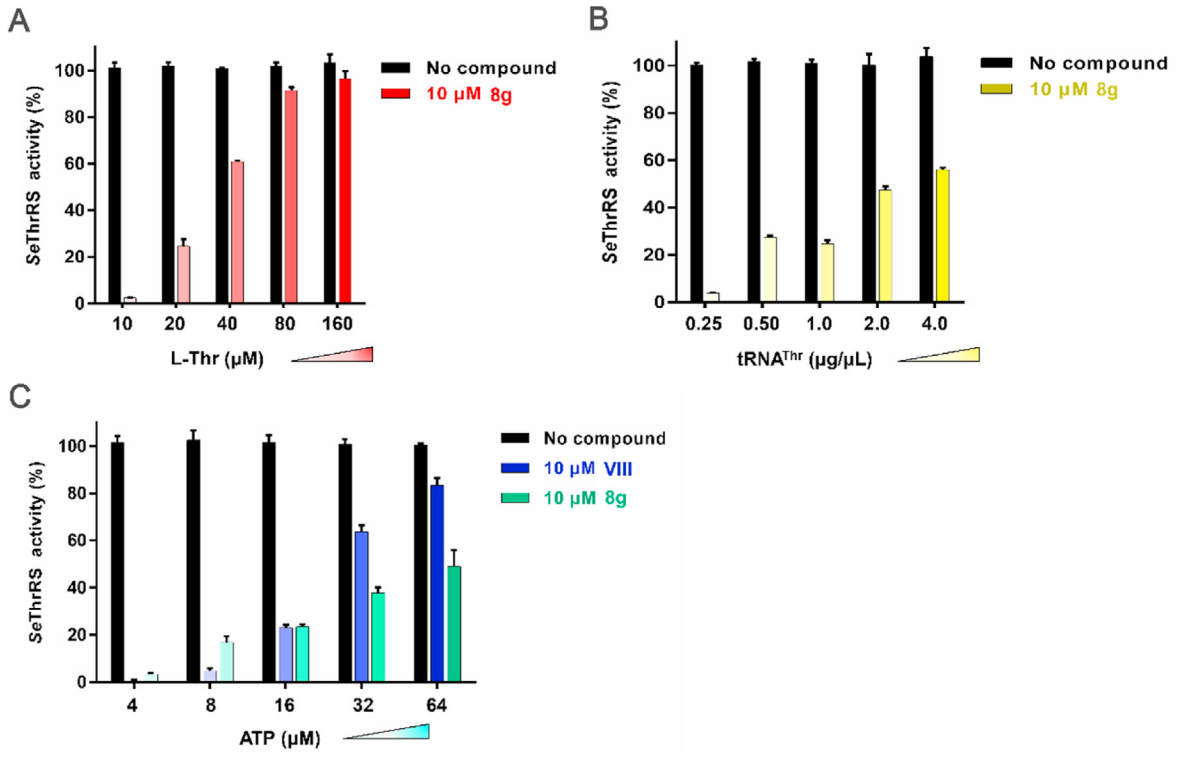

Fig. 7. Competition of compound **8g** with the three substrates of *Se*ThrRS. (A) The inhibition of *Se*ThrRS enzymatic activity by 10 μM compound **8g** was gradually reversed by increasing the concentration of L-Thr. (B) The increase in $tRNA^{Thr}$ concentration recovered the *Se*ThrRS enzymatic activity inhibited by 10 μM compound **8g**. (C) The increase in ATP concentration recovered the *Se*ThrRS enzymatic activity inhibited by 10 μM **VIII** or 10 μM compound **8g**.

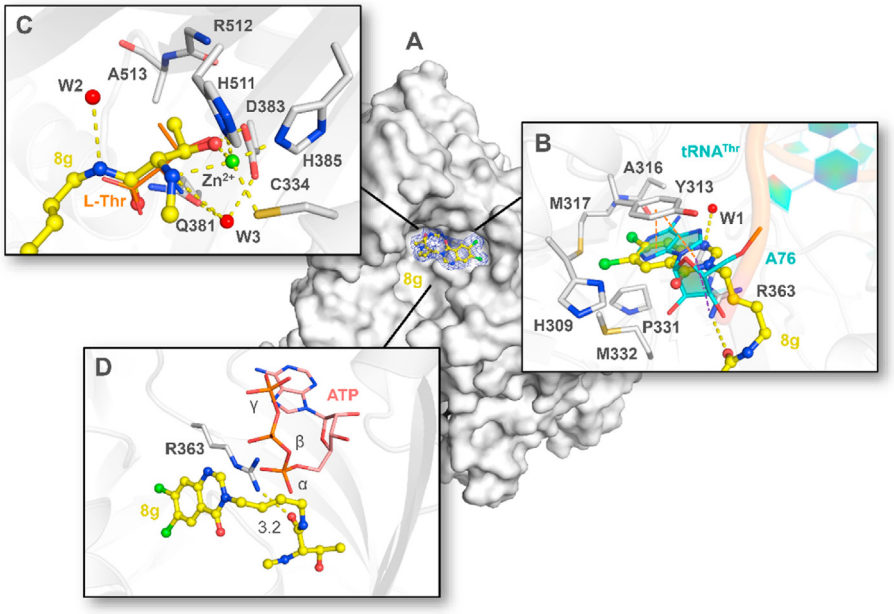

Fig. 8. Compound **8g** (yellow, PDB code: 7CBG) interfered with the three substrates of ThrRS for the aminoacylation reaction. (A) Compound **8g** occupies the active site of *Se*ThrRS. (B) Close-up view of the $tRNA^{Thr}$ binding pocket. The structure of the *Se*ThrRS-**8g** complex was superimposed with that of the *Escherichia coli* ThrRS-$tRNA^{Thr}$ complex (cyan, PDB code: 1QF6). (C) Close-up view of the L-Thr binding pocket. The structure of the *Se*ThrRS-**8g** complex was superimposed with that of the *E. coli* ThrRS-L-Thr complex (orange, PDB code: 1EVK). (D) Close-up view of the ATP binding pocket. The structure of the *Se*ThrRS-**8g** complex was superimposed with that of the *Staphylococcus aureus* ThrRS-ATP complex (pink, PDB code: 1NYR). The $2F_o$-F_c composite density map is contoured at 1σ and drawn as a blue mesh; water molecules are shown as red spheres; zinc ion is shown as a light green sphere; hydrogen bonds are shown as yellow dashed lines; cation-π interactions are shown as a purple dashed line; and π-π stacking interactions are shown as orange dashed lines. (For interpretation of the references to colour in this figure legend, the reader is referred to the Web version of this article.)

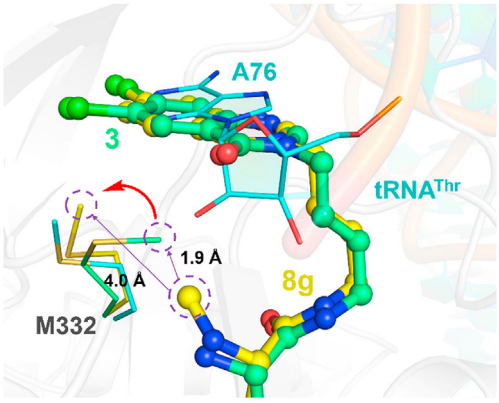

Fig. 9. Comparison of the Met332 side chain conformation induced by inhibitor **3** (green), compound **8g** (yellow) and A76 of $tRNA^{Thr}$ (cyan). The conformation of the side chain of Met332 in the **8g**-bound state (yellow) is similar to that of the $tRNA^{Thr}$-bound state (cyan), but distinct to that of the **3**-bound state (green). The distances between the methyl group on the α-NH_2 of compound **8g** and the terminal methyl group of Met332 in both the **8g**-bound state and the **3**-bound state are labeled. (For interpretation of the references to colour in this figure legend, the reader is referred to the Web version of this article.)

Table 3
MIC values of compounds **8g**, **9a** and **9b** against several bacterial strains.

Compound	MIC (μg/mL)					
	Gram-positive bacteria			Gram-negative bacteria		
	S. aureus	MRSA	*E. faecalis*	*E. coli*	*S. enterica*	*P. aeruginosa*
8g	32	32	32	16	16	32
9a	64	32	32	16	32	32
9b	32	64	32	32	32	64
VIII	>256	>256	>256	>256	>256	>256
HF	64	64	128	128	64	64
Ampicillin	NT[a]	NT	NT	1	1	0.5
Vancomycin	1	2	2	NT	NT	NT

[a]NT, not tested.

extracted with EtOAc (3 × 20.0 mL). The combined organic layers were washed with brine (3 × 20.0 mL), dried with anhydrous Na_2SO_4, filtered, and concentrated under vacuum. The product (1.07 g, 3.46 mmol) and triphenylphosphine (1.18 g, 4.50 mmol) in anhydrous THF (20.0 mL) were stirred at 25 °C for 30 min. Water (3 mL) was added dropwise, and the mixture was stirred at room temperature overnight. The reaction mixture was concentrated *in vacuo*, and the crude product was purified by flash silica gel column chromatography (CH_2Cl_2/MeOH = 4/1) to afford **7** (833 mg, 85%) as a yellow solid.

*4.2.3. General synthetic procedure for the preparation of **3** and **8a-g** (with **8g** as an example)*

To a solution of **7** (50 mg, 0.177 mmol), *N*-(*tert*-butoxycarbonyl)-*N*-methyl-L-Thr (62 mg, 0.266 mmol) and HATU (100 mg, 0.266 mmol) in DMF (3 mL), was added DIPEA (45.7 mg, 0.354 mmol) dropwise at 0 °C, and the mixture was stirred at room temperature for 2 h. The resulting mixture was quenched with water and the aqueous solution was extracted with EtOAc (3 × 5.0 mL). The combined organic layers were washed with brine (3 × 5.0 mL), dried with anhydrous Na_2SO_4, filtered, and concentrated under vacuum to give the crude product. The crude product was purified by silica gel column chromatography (hexane/CH_2Cl_2 = 2/1) to afford Boc protected intermediate (76.5 mg, 87%) as a white solid. To a solution of the crude product (50 mg, 0.0602 mmol) in dioxane (1 mL), 4 N HCl dioxane solution (1.0 mL) was added dropwise, and the resulting mixture was stirred at room temperature for 2 h. The reaction mixture was concentrated *in vacuo*, and the crude product was purified by flash silica gel column chromatography (CH_2Cl_2/MeOH = 5/1) to afford **8g** (34.0 mg, 85%) as a white solid.

4.2.3.1. (2S,3R)-2-amino-N-((E)-4-(6,7-dichloro-4-oxoquinazolin-3(4H)-yl)but-2-en-1-yl)-3-hydroxybutanamide (**3**). White solid, 90%. ^{1}H NMR (500 MHz, MeOD) δ 8.29 (d, *J* = 34.7 Hz, 2H), 7.83 (s, 1H), 5.91–5.78 (m, 2H), 4.63 (d, *J* = 3.8 Hz, 2H), 3.91 (d, *J* = 5.7 Hz, 1H), 3.85 (d, *J* = 3.5 Hz, 2H), 3.09 (d, *J* = 4.5 Hz, 1H), 1.14 (d, *J* = 6.4 Hz, 3H). ESI-MS: *m/z* 385.1 $[M+H]^+$.

4.2.3.2. (S,E)-N-(4-(6,7-dichloro-4-oxoquinazolin-3(4H)-yl)but-2-en-1-yl)-5-oxopyrrolidine-2-carboxamide (**8a**). White solid, 92%. ^{1}H NMR (400 MHz, DMSO) δ 8.43 (s, 1H), 8.25 (s, 1H), 8.13 (t, *J* = 5.5 Hz, 1H), 7.99 (s, 1H), 7.78 (s, 1H), 5.77–5.67 (m, 2H), 4.58 (d, *J* = 4.6 Hz, 2H), 3.96 (dd, *J* = 8.4, 4.4 Hz, 1H), 3.69 (d, *J* = 4.5 Hz, 2H), 2.28–2.18 (m, 1H), 2.14–2.02 (m, 2H), 1.83 (ddd, *J* = 13.4, 9.7, 5.2 Hz, 1H). ^{13}C NMR (101 MHz, DMSO) δ 177.79, 172.69, 158.96, 149.95, 147.85, 137.64, 131.59, 130.19, 129.41, 127.84, 125.09, 122.06, 56.20, 47.42, 39.98, 29.70, 25.79. HR-ESI-MS: $[M+H]^+$ *m/z* = 395.0672, calcd for $C_{16}H_{20}N_4O_3$, found 395.0612.

4.2.3.3. (R,E)-N-(4-(6,7-dichloro-4-oxoquinazolin-3(4H)-yl)but-2-en-1-yl)-5-oxopyrrolidine-2-carboxamide (**8b**). White solid, 90%. ^{1}H NMR (500 MHz, DMSO) δ 8.43 (s, 1H), 8.24 (s, 1H), 8.17 (s, 1H), 7.98 (s, 1H), 7.79 (s, 1H), 5.76–5.66 (m, 2H), 4.58 (s, 2H), 3.98 (d, *J* = 3.7 Hz, 1H), 3.70 (s, 2H), 2.26–2.19 (m, 1H), 2.10 (td, *J* = 16.1, 8.1 Hz, 2H), 1.83 (s, 1H). ^{13}C NMR (126 MHz, DMSO) δ 177.78, 172.68, 158.95, 149.95, 147.85, 137.63, 131.61, 130.18, 129.40, 127.83, 125.10, 122.05, 56.20, 47.42, 40.08, 29.71, 25.77. HR-ESI-MS: $[M+H]^+$ *m/z* = 395.0672, calcd for $C_{16}H_{20}N_4O_3$, found 395.0612.

4.2.3.4. (2R,3S)-2-amino-N-((E)-4-(6,7-dichloro-4-oxoquinazolin-3(4H)-yl)but-2-en-1-yl)-3-hydroxybutanamide (**8c**). White solid, 87%. ^{1}H NMR (500 MHz, DMSO) δ 8.42 (s, 1H), 8.22 (s, 1H), 8.02 (s, 1H), 7.96 (s, 1H), 5.77–5.66 (m, 2H), 4.57 (s, 2H), 3.78–3.66 (m, 3H), 2.90 (s, 1H), 1.00 (d, *J* = 5.7 Hz, 3H). ^{13}C NMR (126 MHz, DMSO) δ 173.73, 158.93, 149.92, 147.83, 137.59, 131.98, 130.15, 129.37, 127.81, 124.94, 122.04, 68.09, 61.05, 47.42, 39.92, 20.63. HR-ESI-MS: $[M+H]^+$ *m/z* = 385.0829, calcd for $C_{16}H_{20}N_4O_3$, found 385.0773.

4.2.3.5. (S,E)-2-amino-N-(4-(6,7-dichloro-4-oxoquinazolin-3(4H)-yl)but-2-en-1-yl)-3-hydroxy-3-methylbutanamide (**8d**). White solid, 85%. ^{1}H NMR (500 MHz, MeOD) δ 8.25 (d, *J* = 38.4 Hz, 2H), 7.78 (s, 1H), 5.91–5.79 (m, 2H), 4.63 (d, *J* = 5.6 Hz, 2H), 3.85 (d, *J* = 4.7 Hz, 2H), 3.15 (s, 1H), 1.18 (s, 3H), 1.16 (s, 3H). ^{13}C NMR (126 MHz, MeOD) δ 173.86, 159.24, 148.91, 147.09, 138.28, 130.99, 130.96, 128.38, 127.36, 125.19, 121.48, 71.33, 63.08, 47.33, 39.88, 25.09, 24.56. HR-ESI-MS: $[M+H]^+$ *m/z* = 399.0985, calcd for $C_{16}H_{20}N_4O_3$, found 399.0931.

4.2.3.6. (S,E)-2-amino-N-(4-(6,7-dichloro-4-oxoquinazolin-3(4H)-yl)but-2-en-1-yl)-3-hydroxypropanamide (**8e**). White solid, 88%. ^{1}H NMR (500 MHz, MeOD) δ 8.28 (s, 1H), 8.24 (s, 1H), 7.80 (s, 1H), 5.87–5.81 (m, 2H), 4.63 (d, *J* = 4.5 Hz, 2H), 3.86 (d, *J* = 3.6 Hz, 2H), 3.65 (t, *J* = 5.6 Hz, 2H), 3.36 (t, *J* = 5.6 Hz, 1H). ^{13}C NMR (126 MHz, MeOD) δ 174.14, 159.31, 148.92, 147.10, 138.28, 131.12, 130.96, 128.37, 127.38, 124.75, 121.51, 64.13, 56.52, 47.35, 39.91. HR-ESI-MS: $[M+H]^+$ *m/z* = 371.0672, calcd for $C_{16}H_{20}N_4O_3$, found 371.0622.

4.2.3.7. (2S,3R)-2-amino-N-((E)-4-(6,7-dichloro-4-oxoquinazolin-3(4H)-yl)but-2-en-1-yl)-3-ethoxybutanamide (**8f**). White solid, 88%. ^{1}H NMR (500 MHz, MeOD) δ 8.28 (d, *J* = 4.8 Hz, 2H), 7.82 (s, 1H), 5.87–5.77 (m, 2H), 4.64 (d, *J* = 4.1 Hz, 2H), 3.85 (d, *J* = 3.7 Hz, 2H), 3.63–3.56 (m, 1H), 3.28 (s, 3H), 3.17 (d, *J* = 4.3 Hz, 1H), 1.13 (d, *J* = 6.3 Hz, 3H). ^{13}C NMR (126 MHz, MeOD) δ 174.12, 159.28, 148.93, 147.15, 138.31, 131.02, 130.97, 128.41, 127.39, 124.81, 121.54, 77.86, 59.24, 55.77, 47.30, 39.84, 14.42. HR-ESI-MS: $[M+H]^+$ *m/z* = 399.0985, calcd for $C_{16}H_{20}N_4O_3$, found 399.0942.

4.2.3.8. (2S,3R)-N-((E)-4-(6,7-dichloro-4-oxoquinazolin-3(4H)-yl)

but-2-en-1-yl)-3-hydroxy-2-(methylamino)butanamide (**8g**). White solid, 85%. ^{1}H NMR (400 MHz, MeOD) δ 8.26 (d, J = 18.7 Hz, 2H), 7.81 (s, 1H), 5.92−5.77 (m, 2H), 4.63 (d, J = 4.8 Hz, 2H), 3.86 (d, J = 4.0 Hz, 2H), 3.76 (p, J = 6.4 Hz, 1H), 2.81 (d, J = 6.6 Hz, 1H), 2.31 (s, 3H), 1.13 (d, J = 6.4 Hz, 3H). ^{13}C NMR (101 MHz, MeOD) δ 173.29, 159.28, 148.91, 147.12, 138.30, 131.06, 130.99, 128.39, 127.37, 125.13, 121.52, 70.79, 67.84, 47.39, 39.82, 33.81, 18.79. HR-ESI-MS: $[M+H]^+$ m/z = 399.0985, calcd for $C_{16}H_{20}N_4O_3$, found 399.0937.

4.2.4. General synthetic procedure for the preparation of **9a-e** (with **9a** as an example)

A mixture of NaH (10 mg, 0.25 mmol) and **3** (30 mg, 0.0781 mmol) in anhydrous DMF (1.2 mL) was stirred at room temperature for 1 h. This white suspension was added iodoethane (18.3 mg, 0.117 mmol), and the resulting reaction mixture was stirred at room temperature for 6 h. The resulting mixture was quenched with water, and the aqueous solution was extracted with EtOAc (3 × 3.0 mL). The combined organic layers were washed with brine (3 × 3.0 mL), dried with anhydrous Na_2SO_4, filtered, and concentrated under vacuum to give the crude product. The crude product was purified by flash silica gel column chromatography (CH_2Cl_2/MeOH = 5/1) to afford **9a** (10.3 mg, 32%) as white solid.

4.2.4.1. (2S,3R)-N-((E)-4-(6,7-dichloro-4-oxoquinazolin-3(4H)-yl) but-2-en-1-yl)*-2-(ethylamino)-3-hydroxybutanamide* (**9a**). White solid, 32%. ^{1}H NMR (500 MHz, MeOD) δ 8.28 (s, 1H), 8.23 (s, 1H), 7.80 (s, 1H), 5.87−5.79 (m, 2H), 4.63 (d, J = 4.7 Hz, 2H), 3.85 (d, J = 3.3 Hz, 2H), 3.77 (dd, J = 12.4, 6.2 Hz, 1H), 2.91 (d, J = 6.4 Hz, 1H), 2.59−2.50 (m, 2H), 1.13 (d, J = 6.2 Hz, 3H), 1.06 (t, J = 7.0 Hz, 3H). ^{13}C NMR (126 MHz, MeOD) δ 173.68, 159.24, 148.91, 147.12, 138.29, 131.06, 130.97, 128.39, 127.36, 125.09, 121.50, 68.80, 67.87, 47.37, 42.45, 39.80, 18.76, 13.86. HR-ESI-MS: $[M+H]^+$ m/z = 413.1142, calcd for $C_{16}H_{20}N_4O_3$, found 413.1094.

4.2.4.2. (2S,3R)-N-((E)-4-(6,7-dichloro-4-oxoquinazolin-3(4H)-yl) but-2-en-1-yl)*-2-((2-fluoroethyl)amino)-3-hydroxybutanamide* (**9b**). White solid, 25%. ^{1}H NMR (400 MHz, $CDCl_3$) δ 8.29 (s, 1H), 7.97 (s, 1H), 7.77 (s, 1H), 7.52 (s, 1H), 5.76 (t, J = 3.6 Hz, 2H), 4.56 (s, 2H), 4.51 (d, J = 3.9 Hz, 1H), 4.40 (d, J = 3.5 Hz, 1H), 4.06 (dd, J = 6.2, 4.4 Hz, 1H), 3.90 (s, 2H), 3.00 (dtd, J = 13.2, 8.8, 4.5 Hz, 2H), 2.85 (ddd, J = 15.2, 9.8, 3.6 Hz, 1H), 1.20 (d, J = 6.3 Hz, 3H). ^{13}C NMR (101 MHz, $CDCl_3$) δ 172.00, 158.30, 146.33, 146.03, 138.03, 130.91, 130.51, 128.05, 126.96, 123.98, 120.45, 82.4 (d, J = 166.7 Hz), 67.06, 66.44, 48.25 (d, J = 1.9 Hz), 46.71, 28.67, 18.65. HR-ESI-MS: $[M+H]^+$ m/z = 431.1048, calcd for $C_{16}H_{20}N_4O_3$, found 431.1006.

4.2.4.3. (2S,3R)-N-((E)-4-(6,7-dichloro-4-oxoquinazolin-3(4H)-yl) but-2-en-1-yl)*-3-hydroxy-2-(isopropylamino)butanamide* (**9c**). White oil, 28%. ^{1}H NMR (500 MHz, MeOD) δ 8.28 (d, J = 11.4 Hz, 2H), 7.83 (s, 1H), 5.83 (dt, J = 10.6, 7.6 Hz, 2H), 4.64 (d, J = 5.0 Hz, 2H), 3.85 (s, 2H), 3.79 (dd, J = 12.6, 6.5 Hz, 1H), 3.02 (d, J = 5.9 Hz, 1H), 2.75−2.68 (m, 1H), 1.14 (d, J = 6.1 Hz, 3H), 1.04 (d, J = 6.0 Hz, 3H), 1.00 (d, J = 6.1 Hz, 3H). ^{13}C NMR (126 MHz, MeOD) δ 173.86, 159.26, 148.93, 147.15, 138.32, 131.00, 130.92, 128.41, 127.39, 125.17, 121.53, 67.84, 66.26, 47.35, 39.83, 26.71, 22.12, 20.82, 18.76. HR-ESI-MS: $[M+H]^+$ m/z = 427.1298, calcd for $C_{16}H_{20}N_4O_3$, found 427.1255.

4.2.4.4. (2S,3R)-2-(allylamino)-N-((E)-4-(6,7-dichloro-4-oxoquinazolin-3(4H)-yl)but-2-en-1-yl)*-3-hydroxybutanamide* (**9d**). White solid, 78%. ^{1}H NMR (500 MHz, $CDCl_3$) δ 8.29 (s, 1H), 7.96 (s, 1H), 7.77 (s, 1H), 7.44 (s, 1H), 5.82−5.73 (m, 3H), 5.14 (d, J = 17.1 Hz, 1H), 5.06 (d, J = 10.1 Hz, 1H), 4.56 (s, 2H), 4.00 (d, J = 4.8 Hz, 1H), 3.94−3.85 (m, 2H), 3.22 (d, J = 4.7 Hz, 2H), 2.97 (s, 1H), 1.17 (d, J = 6.0 Hz, 3H). ^{13}C NMR (126 MHz, $CDCl_3$) δ 172.23, 158.28, 146.30, 146.05, 138.04, 134.92, 130.92, 130.61, 128.07, 126.97, 123.97, 120.46, 115.81, 67.10, 65.61, 50.69, 46.71, 39.08, 18.62.HR-ESI-MS: $[M+H]^+$ m/z = 425.1142, calcd for $C_{16}H_{20}N_4O_3$, found 425.1099.

4.2.4.5. (2S,3R)-2-((cyanomethyl)amino)-N-((E)-4-(6,7-dichloro-4-oxoquinazolin-3(4H)-yl)but-2-en-1-yl)*-3-hydroxybutanamide* (**9e**). White solid, 41%. ^{1}H NMR (400 MHz, $CDCl_3$) δ 8.27 (s, 1H), 7.98 (s, 1H), 7.76 (s, 1H), 7.17 (t, J = 5.8 Hz, 1H), 5.77 (d, J = 5.3 Hz, 2H), 4.55 (d, J = 4.5 Hz, 2H), 4.01−3.93 (m, 2H), 3.88 (s, 1H), 3.62 (t, J = 19.5 Hz, 2H), 3.22 (s, 1H), 3.10 (d, J = 5.0 Hz, 1H), 1.23 (s, 3H). ^{13}C NMR (101 MHz, $CDCl_3$) δ 170.27, 158.35, 146.43, 146.00, 138.07, 130.94, 130.18, 128.02, 126.91, 124.35, 120.40, 116.52, 67.10, 66.26, 46.73, 39.37, 35.75, 18.66. HR-ESI-MS: $[M+H]^+$ m/z = 424.0938, calcd for $C_{16}H_{20}N_4O_3$, found 424.0892.

4.3. Thermal shift assay

The affinities of the compounds binding to *Se*ThrRS were firstly evaluated by using a fluorescence-based thermal shift assay (TSA) as previously described. In brief, 100 mM HEPES pH 7.5, 150 mM NaCl, 4 × SYPRO orange fluorescent dye, 8 μM *Se*ThrRS, 0.5 mM compounds (or 0.5% DMSO as blank control) were added into 96 well PCR plate to prepare 20 μL reaction system. The PCR plate was placed in a StepOnePlus real-time fluorescent quantitative PCR instrument (Life Technologies Inc.), and incubated at 25 °C for 10 min. Then, the temperature was raised from 25 °C to 95 °C at a rate of 1 °C/min, and the fluorescent signal was recorded every 30 s during this period. The protein melting temperature (T_m) values were calculated by fitting the curves of fluorescence intensity versus temperature using the StepOne™ software v2.3. The data were the average of three independent experiments.

4.4. Enzyme inhibition assay

The aminoacylation activities of *Se*ThrRS in the presence of different compounds were detected by measuring ATP consumption in the reaction [30]. The 10 μL reaction consisted of 25 nM *Se*ThrRS, 4 μM ATP, 10 μM L-threonine, 500 μg/mL *E. coli* total tRNA, 30 mM HEPES pH 7.5, 150 mM NaCl, 30 mM KCl, 40 mM $MgCl_2$, 1 mM dithiothreitol, 0.1% BSA and 100 μM each compound. The reactions were incubated at room temperature for 3 h, then stopped by adding 10 μL Kinase-Glo® Reagent (Promega Inc.). The luminescence was read on a FlexStation 3 multimode microplate reader (Molecular Devices Inc.). The reactions consisted of three groups: the blank group without compounds, the experimental group with compounds, and the control group without enzyme. The inhibitory rate for each compound was calculated as inhibition rate (%) = $(RLU_{compound} - RLU_{blank})/(RLU_{control} - RLU_{blank}) \times 100\%$. The inhibitory rate was measured in three independent assays, and the average value was provided.

The compounds with an inhibitory rate higher than 50% at 100 μM were further measured for their IC_{50} values. The inhibitory rates of the compounds at various concentrations were measured, and IC_{50} values were calculated by fitting the curves with GraphPad Prism 7 using the function of inhibition rate (%) = $100/(1 + [I]/IC_{50})$ B, where B corresponds to the slope factor and $[I]$ corresponds to the compound concentration.

4.5. Isothermal titration calorimetry

The thermodynamic binding constant of compound **8g** with *Se*ThrRS was determined by isothermal titration calorimetry (ITC). 20 μM *Se*ThrRS and 200 μM compound **8g** were prepared with a buffer containing 20 mM HEPES pH 7.5 and 150 mM NaCl, and loaded onto the sample cell and injection syringe of MicroCal VP-ITC microcalorimeter (MicroCal Inc.), respectively. The injection volume of the first titration was 5 μL, and other 24 injections were 10 μL with a 180 s interval between each injection. The dissociation constant (K_d), thermodynamics of binding (ΔH and ΔS) and stoichiometry of binding (N) were determined by fitting the calorimetric data using ORIGIN software (MicroCal Inc.).

4.6. Determination of the antibacterial activity

MICs were determined by broth microdilution using CLSI (Clinical and Laboratory Standards Institute) conditions. The following strains for susceptibility testing were used in the antibacterial assays: *E. coli* ATCC25922, *S. enterica* 87, *P. aeruginosa* ATCC27853, *S. aureus* ATCC29213, MRSA R3708, and *E. faecalis* ATCC29212. The compounds were assayed against the strains in 2-fold dilutions starting from a concentration of 256 μg/mL. The defined medium used in this study was similar to that described previously [15] and consisted of M9 medium with 0.4% glucose supplemented with 100 μM all canonical amino acids. The MIC was defined as the minimum concentration at which a well showed no obvious growth by visual inspection.

4.7. Molecular docking

MOE (The Molecular Operating Environment, Chemical Computing Group Inc.) Version 2015.10 were employed to perform the docking calculations and to show the energy scoring functions. The three-dimensional structures of all the compounds were generated and optimized by Discovery Studio (BIOVIA Inc.). For the crystal structure of the *Se*ThrRS-compound complexes, hydrogens were added, structural problems addressed, partial charges calculated, and some geometry optimization performed. The virtual receptor-ligand complexes were generated by docking the designed compounds into the active site of *Se*ThrRS. The output scores, ligand strain energies, and docked poses were analyzed using a Database Browser. The docked poses at the active site of *Se*ThrRS were used for graphical representation in PyMOL.

4.8. Protein crystallography

Crystallization was performed using the sitting-drop vapor-diffusion method. *Se*ThrRS (15 mg/mL) was premixed with 4 mM inhibitor **1** or **2** at 4 °C for 2 h, diluted with 1 μL reservoir solution (0.24 M lithium acetate pH 7.5, 18% *w*/*v* PEG3350), and equilibrated against 100 μL reservoir solution at 26 °C. Large crystal appeared after 4 days, and the crystals were flash frozen in liquid nitrogen using the cryoprotectant solution consisting of 0.24 M lithium acetate pH 7.5, 18% *w*/*v* PEG3350 and 20% glycerol. The diffraction data were collected at 100 K at the beamline BL17U1 or BL19U1 of the Shanghai Synchrotron Radiation Facility (SSRF) and processed using XDS [44]. The structure was solved by using the molecular replacement method in Phaser [45] with *Se*ThrRS (PDB code: 6L2P) [32] as the search model. Then, iterative refinements of the structure models were carried out using Coot [46] and Refmac5 [47].

The crystals of *Se*ThrRS-**8g** complex were grown under the same condition as above. The data of *Se*ThrRS-**8g** complex were collected at 100 K on an in-house Oxford Diffraction Xcalibur Nova Synergy diffractometer, and the data were processed using the program *CrysAlis Pro*. The structure of the *Se*ThrRS-inhibitor **3** complex (PDB code: 6L2P) was used as the template to solve the structure of the *Se*ThrRS-**8g** complex. The stereochemical quality of the final model was examined using MolProbity [48]. The data collection and refinement statistics are listed in Supplementary Table S1. The atomic coordinates and structural factors were deposited in the PDB under codes 7CBI, 7CBH and 7CBG for *Se*ThrRS-**1** complex, *Se*ThrRS-**2** complex and *Se*ThrRS-**8g** complex, respectively.

Declaration of competing interest

The authors declare that they have no known competing financial interests or personal relationships that could have appeared to influence the work reported in this paper.

Acknowledgements

The authors thank the staff of BL17U1 and BL19U1 beamlines at Shanghai Synchrotron Radiation Facility (SSRF) for assistance during data collection. This research was supported by National Natural Science Foundation of China (No. 81773636), Guangdong Basic and Applid Basic Foundation (Nos. 2019A1515011571, 2017A030313123), Program for Guangdong Introducing Innovative and Entrepreneurial Teams (No. 2016ZT06Y337), Fundamental Research Funds for Central Universities (No. 36000−31650011), and Guangdong Provincial Key Laboratory of Chiral Molecule and Drug Discovery (No. 2019B030301005), and National Engineering and Technology Research Center for New drug Druggability Evaluation (Seed Program of Guangdong Province, No. 2017B090903004).

Appendix A. Supplementary data

Supplementary data to this article can be found online at https://doi.org/10.1016/j.ejmech.2020.112848.

Author contributions

J.G. and H.Z. designed the research. J.G., B.Chen, Y.Y. and B.Cheng performed the experiments. J.G., Y.J., J.T., Z.C., Q.G. and J.X. analyzed the data. J.G. and H.Z. wrote the paper. All authors approved the final version of the manuscript.

References

[1] M. Ibba, D. Söll, Quality control mechanisms during translation, Science 286 (1999) 1893−1897.
[2] M. Ibba, A.W. Curnow, D. Söll, Aminoacyl-tRNA synthesis: divergent routes to a common goal, Trends Biochem. Sci. 22 (1997) 39−42.
[3] M. Delarue, Aminoacyl-tRNA synthetases, Curr. Opin. Struct. Biol. 5 (1995) 48−55.
[4] U.A. Ochsner, X. Sun, T. Jarvis, I. Critchley, N. Janjic, Aminoacyl-tRNA synthetases: essential and still promising targets for new anti-infective agents, Expet Opin. Invest. Drugs 16 (2007) 573−593.
[5] E.Y. Lee, S. Kim, M.H. Kim, Aminoacyl-tRNA synthetases, therapeutic targets for infectious diseases, Biochem. Pharmacol. 154 (2018) 424−434.
[6] N.H. Kwon, P.L. Fox, S. Kim, Aminoacyl-tRNA synthetases as therapeutic targets, Nature reviews, Drug discovery 18 (2019) 629−650.
[7] G.H. Vondenhoff, A. Van Aerschot, Aminoacyl-tRNA synthetase inhibitors as potential antibiotics, Eur. J. Med. Chem. 46 (2011) 5227−5236.
[8] V. Dewan, J. Reader, K.M. Forsyth, Role of aminoacyl-tRNA synthetases in infectious diseases and targets for therapeutic development, Top. Curr. Chem. 344 (2014) 293−329.
[9] C.S. Francklyn, P. Mullen, Progress and challenges in aminoacyl-tRNA synthetase-based therapeutics, J. Biol. Chem. 294 (2019) 5365−5385.
[10] P. Yao, P.L. Fox, Aminoacyl-tRNA synthetases in medicine and disease, EMBO Mol. Med. 5 (2013) 332−343.
[11] A.T. Fuller, G. Mellows, M. Woolford, G.T. Banks, K.D. Barrow, E.B. Chain, Pseudomonic acid: an antibiotic produced by Pseudomonas fluorescens, Nature 234 (1971) 416−417.
[12] L.F. Silvian, J. Wang, T.A. Steitz, Insights into editing from an ile-tRNA synthetase structure with tRNAile and mupirocin, Science 285 (1999) 1074−1077.
[13] I.A. Critchley, L.S. Green, C.L. Young, J.M. Bullard, R.J. Evans, M. Price, T.C. Jarvis, J.W. Guiles, N. Janjic, U.A. Ochsner, Spectrum of activity and mode of action of REP3123, a new antibiotic to treat Clostridium difficile infections, J. Antimicrob. Chemother. 63 (2009) 954−963.
[14] C.Y. Koh, J.E. Kim, S. Shibata, R.M. Ranade, M. Yu, J. Liu, J.R. Gillespie, F.S. Buckner, C.L. Verlinde, E. Fan, W.G. Hol, Distinct states of methionyl-tRNA synthetase indicate inhibitor binding by conformational selection, Structure 20 (2012) 1681−1691.
[15] D. Beyer, H.P. Kroll, R. Endermann, G. Schiffer, S. Siegel, M. Bauser, J. Pohlmann, M. Brands, K. Ziegelbauer, D. Haebich, C. Eymann, H. Brötz-Oesterhelt, New class of bacterial phenylalanyl-tRNA synthetase inhibitors with high potency and broad-spectrum activity, Antimicrob. Agents Chemother. 48 (2004) 525−532.
[16] A. Abibi, A.D. Ferguson, P.R. Fleming, N. Gao, L.I. Hajec, J. Hu, V.A. Laganas, D.C. McKinney, S.M. McLeod, D.B. Prince, A.B. Shapiro, E.T. Buurman, The role of a novel auxiliary pocket in bacterial phenylalanyl-tRNA synthetase druggability, J. Biol. Chem. 289 (2014) 21651−21662.

[17] J.I. Guijarro, J.E. González-Pastor, F. Baleux, J.L. San Millán, M.A. Castilla, M. Rico, F. Moreno, M. Delepierre, Chemical structure and translation inhibition studies of the antibiotic microcin C7, J. Biol. Chem. 270 (1995) 23520–23532.
[18] A. Metlitskaya, T. Kazakov, A. Kommer, O. Pavlova, M. Praetorius-Ibba, M. Ibba, I. Krasheninnikov, V. Kolb, I. Khmel, K. Severinov, Aspartyl-tRNA synthetase is the target of peptide nucleotide antibiotic Microcin C, J. Biol. Chem. 281 (2006) 18033–18042.
[19] F.L. Rock, W. Mao, A. Yaremchuk, M. Tukalo, T. Crépin, H. Zhou, Y.K. Zhang, V. Hernandez, T. Akama, S.J. Baker, J.J. Plattner, L. Shapiro, S.A. Martinis, S.J. Benkovic, S. Cusack, M.R. Alley, An antifungal agent inhibits an aminoacyl-tRNA synthetase by trapping tRNA in the editing site, Science 316 (2007) 1759–1761.
[20] D. Tworowski, L. Klipcan, M. Peretz, N. Moor, M.G. Safro, Universal pathway for posttransfer editing reactions: insights from the crystal structure of TtPheRS with puromycin, Proc. Natl. Acad. Sci. U.S.A. 112 (2015) 3967–3972.
[21] M.L. Bovee, M.A. Pierce, C.S. Francklyn, Induced fit and kinetic mechanism of adenylation catalyzed by Escherichia coli threonyl-tRNA synthetase, Biochemistry 42 (2003) 15102–15113.
[22] M. Teng, M.T. Hilgers, M.L. Cunningham, A. Borchardt, J.B. Locke, S. Abraham, G. Haley, B.P. Kwan, C. Hall, G.W. Hough, K.J. Shaw, J. Finn, Identification of bacteria-selective threonyl-tRNA synthetase substrate inhibitors by structure-based design, J. Med. Chem. 56 (2013) 1748–1760.
[23] A. Torres-Larios, R. Sankaranarayanan, B. Rees, A.C. Dock-Bregeon, D. Moras, Conformational movements and cooperativity upon amino acid, ATP and tRNA binding in threonyl-tRNA synthetase, J. Mol. Biol. 331 (2003) 201–211.
[24] M. Ibba, D. Soll, Aminoacyl-tRNA synthesis, Annu. Rev. Biochem. 69 (2000) 617–650.
[25] P. Fang, M. Guo, Evolutionary limitation and opportunities for developing tRNA synthetase inhibitors with 5-binding-mode classification, Life 5 (2015) 1703–1725.
[26] H. Belrhali, A. Yaremchuk, M. Tukalo, K. Larsen, C. Berthet-Colominas, R. Leberman, B. Beijer, B. Sproat, J. Als-Nielsen, G. Grübel, et al., Crystal structures at 2.5 angstrom resolution of seryl-tRNA synthetase complexed with two analogs of seryl adenylate, Science 263 (1994) 1432–1436.
[27] A.J. Pope, J. Lapointe, L. Mensah, N. Benson, M.J. Brown, K.J. Moore, Characterization of isoleucyl-tRNA synthetase from Staphylococcus aureus. I: kinetic mechanism of the substrate activation reaction studied by transient and steady-state techniques, J. Biol. Chem. 273 (1998) 31680–31690.
[28] J.G. Hurdle, A.J. O'Neill, I. Chopra, Prospects for aminoacyl-tRNA synthetase inhibitors as new antimicrobial agents, Antimicrob. Agents Chemother. 49 (2005) 4821–4833.
[29] K.J. Saliba, K. Kirk, pH regulation in the intracellular malaria parasite, Plasmodium falciparum. H(+) extrusion via a V-type H(+)-ATPase, J. Biol. Chem. 274 (1999) 33213–33219.
[30] B. Baragaña, B. Forte, R. Choi, S. Nakazawa Hewitt, J.A. Bueren-Calabuig, J.P. Pisco, C. Peet, D.M. Dranow, D.A. Robinson, C. Jansen, N.R. Norcross, S. Vinayak, M. Anderson, C.F. Brooks, C.A. Cooper, S. Damerow, M. Delves, K. Dowers, J. Duffy, T.E. Edwards, I. Hallyburton, B.G. Horst, M.A. Hulverson, L. Ferguson, M.B. Jiménez-Díaz, R.S. Jumani, D.D. Lorimer, M.S. Love, S. Maher, H. Matthews, C.W. McNamara, P. Miller, S. O'Neill, K.K. Ojo, M. Osuna-Cabello, E. Pinto, J. Post, J. Riley, M. Rottmann, L.M. Sanz, P. Scullion, A. Sharma, S.M. Shepherd, Y. Shishikura, F.R.C. Simeons, E.E. Stebbins, L. Stojanovski, U. Straschil, F.K. Tamaki, J. Tamjar, L.S. Torrie, A. Vantaux, B. Witkowski, S. Wittlin, M. Yogavel, F. Zuccotto, I. Angulo-Barturen, R. Sinden, J. Baum, F.J. Gamo, P. Mäser, D.E. Kyle, E.A. Winzeler, P.J. Myler, P.G. Wyatt, D. Floyd, D. Matthews, A. Sharma, B. Striepen, C.D. Huston, D.W. Gray, A.H. Fairlamb, A.V. Pisliakov, C. Walpole, K.D. Read, W.C. Van Voorhis, I.H. Gilbert, Lysyl-tRNA synthetase as a drug target in malaria and cryptosporidiosis, Proc. Natl. Acad. Sci. U.S.A. 116 (2019) 7015–7020.
[31] B.D. Bennett, E.H. Kimball, M. Gao, R. Osterhout, S.J. Van Dien, J.D. Rabinowitz, Absolute metabolite concentrations and implied enzyme active site occupancy in Escherichia coli, Nat. Chem. Biol. 5 (2009) 593–599.
[32] J. Guo, B. Chen, Y. Yu, B. Cheng, Y. Cheng, Y. Ju, Q. Gu, J. Xu, H. Zhou, Discovery of novel tRNA-amino acid dual-site inhibitors against threonyl-tRNA synthetase by fragment-based target hopping, Eur. J. Med. Chem. 187 (2020) 111941.
[33] R. Sankaranarayanan, A.C. Dock-Bregeon, P. Romby, J. Caillet, M. Springer, B. Rees, C. Ehresmann, B. Ehresmann, D. Moras, The structure of threonyl-tRNA synthetase-tRNA(Thr) complex enlightens its repressor activity and reveals an essential zinc ion in the active site, Cell 97 (1999) 371–381.
[34] R. Sankaranarayanan, A.C. Dock-Bregeon, B. Rees, M. Bovee, J. Caillet, P. Romby, C.S. Francklyn, D. Moras, Zinc ion mediated amino acid discrimination by threonyl-tRNA synthetase, Nat. Struct. Biol. 7 (2000) 461–465.
[35] P. Asadi, G. Khodarahmi, A. Jahanian-Najafabadi, L. Saghaie, F. Hassanzadeh, Biologically active heterocyclic hybrids based on quinazolinone, benzofuran and imidazolium moieties: synthesis, characterization, cytotoxic and antibacterial evaluation, Chem. Biodivers. 14 (2017).
[36] N.P. McLaughlin, P. Evans, Dihydroxylation of vinyl sulfones: stereoselective synthesis of (+)- and (-)-febrifugine and halofuginone, J. Org. Chem. 75 (2010) 518–521.
[37] C. Zhao, D. Huang, R. Li, Y. Xu, S. Su, Q. Gu, J. Xu, Identifying novel anti-osteoporosis leads with a chemotype-assembly approach, J. Med. Chem. 62 (2019) 5885–5900.
[38] M. Sarkis, D.N. Tran, S. Kolb, M.A. Miteva, B.O. Villoutreix, C. Garbay, E. Braud, Design and synthesis of novel bis-thiazolone derivatives as micromolar CDC25 phosphatase inhibitors: effect of dimerisation on phosphatase inhibition, Bioorg. Med. Chem. Lett 22 (2012) 7345–7350.
[39] Z. Lin, X. Xu, S. Zhao, X. Yang, J. Guo, Q. Zhang, C. Jing, S. Chen, Y. He, Total synthesis and antimicrobial evaluation of natural albomycins against clinical pathogens, Nat. Commun. 9 (2018) 3445.
[40] F.H. Niesen, H. Berglund, M. Vedadi, The use of differential scanning fluorimetry to detect ligand interactions that promote protein stability, Nat. Protoc. 2 (2007) 2212–2221.
[41] T.M. Mezzasalma, J.K. Kranz, W. Chan, G.T. Struble, C. Schalk-Hihi, I.C. Deckman, B.A. Springer, M.J. Todd, Enhancing recombinant protein quality and yield by protein stability profiling, J. Biomol. Screen 12 (2007) 418–428.
[42] X. Huang, J. Guo, Q. Liu, Q. Gu, J. Xu, H. Zhou, Identification of an auxiliary druggable pocket in the DNA gyrase ATPase domain using fragment probes, MedChemComm 9 (2018) 1619–1629.
[43] H. Zhou, L. Sun, X.L. Yang, P. Schimmel, ATP-directed capture of bioactive herbal-based medicine on human tRNA synthetase, Nature 494 (2013) 121–124.
[44] W. Kabsch, XDS, Acta Crystallogr D Biol Crystallogr 66 (2010) 125–132.
[45] A.J. McCoy, Solving structures of protein complexes by molecular replacement with Phaser, Acta Crystallogr D Biol Crystallogr 63 (2007) 32–41.
[46] P. Emsley, B. Lohkamp, W.G. Scott, K. Cowtan, Features and development of Coot, Acta Crystallogr D Biol Crystallogr 66 (2010) 486–501.
[47] G.N. Murshudov, A.A. Vagin, E.J. Dodson, Refinement of macromolecular structures by the maximum-likelihood method, Acta Crystallogr D Biol Crystallogr 53 (1997) 240–255.
[48] V.B. Chen, W.B. Arendall 3rd, J.J. Headd, D.A. Keedy, R.M. Immormino, G.J. Kapral, L.W. Murray, J.S. Richardson, D.C. Richardson, MolProbity: all-atom structure validation for macromolecular crystallography, Acta Crystallogr D Biol Crystallogr 66 (2010) 12–21.